Extensions of Quartz-Enhanced Photoacoustic Spectroscopy

by

Amrita V. Masurkar

Submitted to the Department of Physics
in partial fulfillment of the requirements for the degree of

Bachelor of Science in Physics

at the

MASSACHUSETTS INSTITUTE OF TECHNOLOGY

June 2009

Author .....
Department of Physics
May 08, 2009

Certified by .....
Rajeev Ram
Professor of Electrical Engineering
Thesis Supervisor

Certified by .....
Marin Soljacic
Assistant Professor of Physics
Thesis Supervisor

Accepted by .....
David E. Pritchard
Senior Thesis Coordinator, Department of Physics

Extensions of Quartz-Enhanced Photoacoustic Spectroscopy

by

Amrita V. Masurkar

Submitted to the Department of Physics
on May 08, 2009, in partial fulfillment of the
requirements for the degree of
Bachelor of Science in Physics

Abstract

The goal of this thesis was to perform quartz-enhanced photoacoustic spectroscopy (QEPAS) on trace concentrations of NH_3 in the 1.53 μm region with a DFB laser without the use of a resonating cavity. I analyzed the process of QEPAS both analytically and experimentally. First, absorption spectroscopy was performed with a 1.55 μm DFB laser on the 1558.033 nm absorption line of $H^{13}C^{12}N$. The wavelength of the laser radiation was then modulated, and the spectral components of the absorbance were analyzed.

In addition, low concentrations of NH_3 were generated through the use of a vacuum system, and absorption spectoscopy was performed on these samples. A tuning fork was also characterized. Photoacoustic signals were ultimately not realized, however, plans for future work are mentioned.

Thesis Supervisor: Rajeev Ram
Title: Professor of Electrical Engineering

Thesis Supervisor: Marin Soljacic
Title: Assistant Professor of Physics

Acknowledgments

First, I would like to thank Professor Rajeev Ram for giving me the opportunity to work at the Research Laboratory of Electronics (RLE), for teaching me what it means to work in a real laboratory and work on a long-term experimental project. He nurtured me to understand every part of my thesis, and to learn something at every point in the project. I would also like to thank Dr. Harry Lee, whose guidance made this thesis possible. A big thank you also goes out to all the members of the laboratory, who were always willing to answer my questions.

I would also like to thank my family and friends for their support for the past five years, whether it was in the form of providing me with deep conversations at odd times of the night or driving to Cambridge every week to provide me with sustainance.

Contents

List of Figures

List of Tables

Chapter 1

Introduction

The purpose of this section is to describe the goals of this thesis and to provide a background of photoacoustic spectroscopy, its history, applications, and theory.

1.1 Strategy

The ultimate objective of this project is to perform quartz-enhanced photoacoustic spectroscopy (QEPAS) on trace amounts of NH_3 without the use of a resonating cavity, and to achieve sensitivity levels on the order of parts per billion (ppb). This process will entail 1.) analyzing methods of laser radiation modulation and absorption spectra of various molecular species, and 2.) determining optimal values for key parameters such as modulation depth in order to generate the largest photoacoustic signal possible.

1.2 Goal

The goals of this thesis was to understand the QEPAS process and, specifically, to perform the following tasks:

- Characterizing the light source (tunable diode laser)
- Analyzing absorbance modulation

- Optically analyzing samples
- Characterizing a quartz-crystal tuning fork
- Creating trace samples of NH_3
- Achieving QEPAS signals
- Determining the concentration range for which QEPAS is valid

1.3 Background of Photoacoustic Spectroscopy (PAS)

1.3.1 Brief History

The photoacoustic (PA) effect was discovered by Alexander Grahm Bell in 1880, when he found that sunlight intermittently hitting an enclosed solid attached to a hearing tube generated sound. He and his contemporaries, Preece, Tyndall and, proved that liquids and gases produced these sounds as well. However, due to limitations in technology, namely amplifiers, sensitive pressure transducers and lasers, few pursued the subject further; Viegerov is named most in the literature as having in 1938 refined Rontgen's and Tyndall's PA gas analysis process [8]. Then in the 1960's with the advent of sensitive microphones and lasers, PAS on trace gas concentrations took off; Atwood and Kerr in 1968 and Kreuzer in 1971 [8]. In addition, Rosencwaig and Gersho in the 1970's modeled the photoacoustic effect in solids [20]. Regarding the history of PAS beyond the 1970's, breakthroughs in PAS have always depended heavily on laser technology. With the availability of the tunable diode laser in the 1980's, for instance, PAS precision increased, due to the narrow linewidth and tunability of the tunable diode laser.

1.3.2 Applications of PAS

PAS has been applied to solids, liquids, and gases in such areas as pollution monitoring, medicine, industrial process control, biology, and earth science. In particular,

there has been an increasing demand for research in trace gas sensing, the applications of which include atmospheric chemistry, volcanic activity, agriculture, industrial processes, workplace surveillance, and medical diagnostics. For instance, PAS has been used to monitor NO from exhaust emissions, which contributes to respiratory allergic diseases, bronchial asthma and the depletion of ozone [9]. In medicine, PAS has been used to monitor drug diffusion rates in skin [3] and to detect trace concentrations of disease biomarkers, such as ethene C_2H_4, ethane C_2H_6, and pentane C_5H_{12}, which are emitted by UV-exposed skin [7], and NO, which is a mark of inflammatory lung diseases [6]. Other applications range from monitoring respiratory NH_3 in cockroaches to detecting the intake of prohibited substances by athletes [14].

Low cost portable PAS sensors have already been on the market, examples of which include smoke detectors, toxic gas monitors, and oil sensors for monitoring hydrocarbons in water. On the academic side, researchers are focused on fine-tuning the precision of PAS and on its miniaturization [13].

1.3.3 Sensitivity

Unlike absorption spectroscopy, PAS is used primarily for detecting trace concentrations (ppm/ppb). Table 1.1 summarizes the sensitivity levels attained by recent studies. All six studies used wavelength modulation and a resonating cavity.

Species	Line (μ m)	Laser	Transducer	Sensitivity	Source
NH_3	1.53	DFB	Quartz Tuning Fork	0.65 ppm	[16]
H_2CO	3.53	Cascade	Quartz Tuning Fork	0.6 ppm	[10]
NH_3	1.53	DFB	Microphone	3.14 ppm	[11]
CH_4	1.65	DFB	Microphone	0.3 ppm	[12]
NH_3	1.53	DFB	Microphone	0.2 ppm	[21]
CO_2	2.74	DFB	Microphone	30 ppb	[23]

Table 1.1: PAS sensitivity levels for various studies.

A scan of the literature suggests that wavelength modulation and resonating cavities are the best options for PAS, and that techniques involving QEPAS are capable of achieving sensitivity levels as low as those using traditional PAS and microphones.

In addition, PAS appears to be used mostly for molecular species whose absorption bands are in the infrared (IR). These studies also show that limitations in achieving a high sensitivity include the linewidth of the laser, selectivity of the line (isolation of a line from those of interfering species), and laser power. In addition, noise sources in the electronics, absorption at cavity walls, and loss of power through coupling contribute to lowering the PAS signal-to-noise ratio (SNR).

1.4 PAS Setup and Theory

1.4.1 Overview

PAS is a calorimetric method, and can be broken down into five main processes as illustrated in Figure 1. Modulated laser light passes through an enclosed sample, which absorbs the radiation. The optical energy is then converted to heat by molecular absorption of photons at the proper wavelength and subsequent non-radiative relaxation of the excited state (collisional relaxation). This absorption causes thermal expansion and induces an acoustic wave, which excites a transducer. In traditional PAS a microphone is typically used, while in quartz-enhanced PAS (QEPAS), the transducer is a quartz-crystal tuning fork which outputs a voltage signal via the piezoelectric effect. The output signal from the transducer is then analyzed to determine the concentration of the sample. Although PAS can be applied to gases, liquids and solids, the highest signal-to-noise ratio can be achieved with the former due to their low viscosities.

1.4.2 Absorption Lines

Without broadening due to transition lifetimes, collisions (pressure), and the distribution of particle velocities (Doppler), an absorption line would be infinitely thin (i.e., a delta function). In reality, however, due to a finite transition lifetime, absorption lines have an inherent Lorentzian shape of the form:

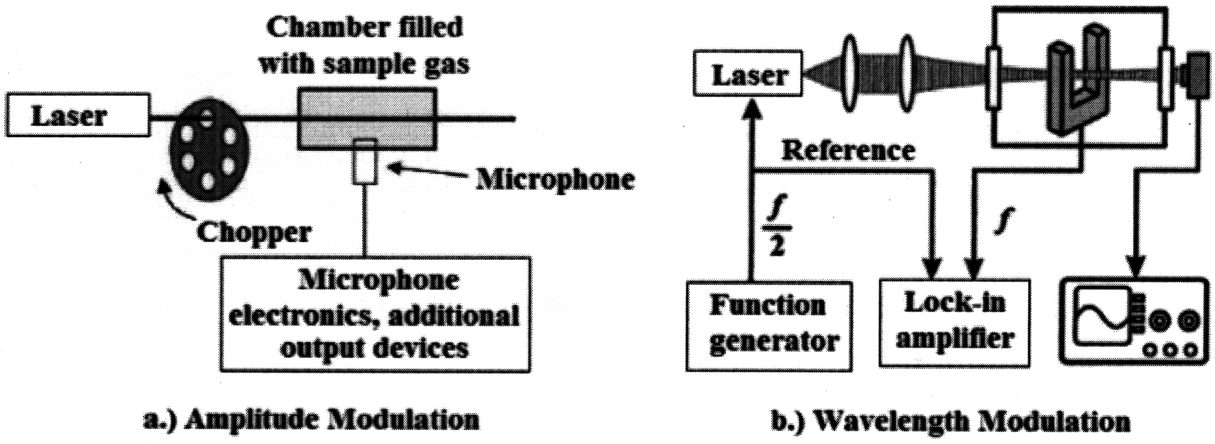

Figure 1-1: Basic Setup of PAS. Light is modulated either through amplitude modulated (left), or by wavelength modulation (right), and is passed through a sample which contains a pressure transducer (microphone or tuning fork) [5].

$$\alpha(\lambda) = \frac{1}{\pi} \frac{\frac{1}{2}\Gamma}{(\lambda - \lambda_0)^2 + \Gamma^2} \tag{1.1}$$

with a width at half-height (WHH) equal to Γ, maximum value $\frac{2}{\pi\Gamma}$, and resonance at λ_0. The atomic decay time τ is related to Γ:

$$\tau = \frac{1}{2\Gamma}. \tag{1.2}$$

Typical values of τ range from 10^{-8} to 10^{-9} s [15], corresponding to Γ values of 10^8 to 10^9 s^{-1}. The absorption coefficient is also related to the absorption cross-section, σ, given by:

$$\alpha(\lambda) = N\sigma(\lambda) \tag{1.3}$$

where N is the concentration in mol/cm^3 or $particles/cm^3$, and σ is in cm^2 and is also a Lorentzian. In practice, however, with the addition of homogeneous Doppler and pressure broadening, the lineshape becomes considerably more complex than a simple Lorenztian. Depending on the state of the absorbing material (temperature and pressure), one type of broadening may dominate over another, thus the line-

shape can be modeled using either a Gaussian or Lorenztian. For instance, at low enough pressures, Doppler broadening and transition lifetime dominate, and the line-shape becomes a convolution of a Lorentzian and Gaussian (Voigt profile). At higher pressures, collisional broadening typically dominates.

1.4.3 Heat and Pressure Wave Generation

The heat generated in a sample by a laser can be derived using rate equations [1]. In a species with two vibrational energy levels and a density of N electrons per unit volume, the rate of electrons in the higher energy level (N') is given by:

$$\frac{dN'}{dt} = (N - N')\sigma\phi - N'\sigma\phi - \frac{N'}{\tau} \tag{1.4}$$

where σ is the absorption cross section of the species in units of area, ϕ is the photon flux rate in units of photons per unit area per unit time, and τ is the transition lifetime in units of time and is defined as

$$\tau^{-1} = \tau_n^{-1} + \tau_r^{-1} \tag{1.5}$$

where τ_n^{-1} and τ_r^{-1} are the nonradiative and radiative time constants, respectively. The first term on the left of Eq. 1.4 is attributed to electronic excitation, the second to stimulated emission, and the third to spontaneous relaxation. Assuming that the number of electrons in the higher energy level is much lower than that in the lower energy level, and that the photon flux is sinusoidal, the rate equation becomes

$$\frac{dN}{dt} = N\sigma\phi_0(1 + e^{i\omega t}) - \frac{N'}{\tau} \tag{1.6}$$

with a solution

$$N' = \frac{N\sigma\phi_0\tau}{\sqrt{1 + (\omega\tau)^2}} e^{i(\omega t - \varphi)} \tag{1.7}$$

where φ is the phase lag between the photon source and N'. The heat generated by the photon flux is:

$$H = N' \frac{h\nu}{\tau_n} \tag{1.8}$$

where $h\nu$ is the average energy due to nonradiative deexcitation. If the period of the photon flux is much greater than τ, and it is assumed that the frequency of the laser is chosen such that $\nu = \nu_{laser}$, then the heat becomes

$$H_0 = N\sigma W_0 = \alpha W_0 \tag{1.9}$$

where H_0 is the heating in W/m^3, α is the absorption coefficient in m^{-1}, and W_0 is the light intensity in W/m^2. As mentioned before, typical values of τ range from 10^{-8} s to 10^{-9} s, whereas PAS modulation frequencies are typically in kHz. From this it is clear that a strong signal can be attained by using a high intensity laser and modulating the wavelength around a peak absorption line.

The heat then acts as a driving force, causing the medium in the immediate vicinity of the beam to expand and contract. The equation for the pressure inside the cavity is [13]:

$$\nabla^2 p - \frac{1}{c_s^2} \frac{\partial^2 p}{\partial^2 t} = -\frac{(\gamma - 1)}{c_s^2} \frac{\partial H}{\partial t} \tag{1.10}$$

where p is the acoustic pressure, H is the heating from (8), c_s is the speed of sound in the sample, and γ is the ratio of the specific heat at constant pressure to that at constant volume. The solution is a superposition of modes in the longitudinal, radial and azimuthal directions (see Figure 2):

$$p(r, \omega) = \Sigma A_j(\omega) p_j(r) \tag{1.11}$$

For a cylindrical cavity of length L and radius R, p_j and the coefficients A_j are given by

$$p_j(r, \phi, z) = cos(m_\phi \phi) cos(k_z z) J_m(k_z r) \tag{1.12}$$

$$A_j(\omega) = \frac{-j\omega}{\omega_j^2} \frac{[(\gamma - 1)/V_c] \int p_j * H dv}{[1 - \omega^2/\omega_j^2 - j\omega/\omega_j Q_j]} \tag{1.13}$$

$$\omega_j = c_s \sqrt{k_z^2 + k_r^2},\ k_z = \frac{\pi}{L} n_z,\ k_r = \frac{\pi}{R} \alpha_{mn} \tag{1.14}$$

where J_m is a Bessel function of the first kind, and m and n are positive integers. In resonant mode, the driving frequency ω from Eq. 1.6 is chosen such that it is equal to one of the resonant frequencies, as a way of amplifying the signal. In non-resonant mode, the driving frequency ω is much less than the lowest resonant frequency of the cavity. In this case, only the first term of the summation in Eq. 1.11 is kept, and the pressure reduces to

$$p(r, \omega) = A_0(\omega) p_0(r) = \frac{i\alpha(\gamma - 1) W_0 L}{\omega V_c}, \tag{1.15}$$

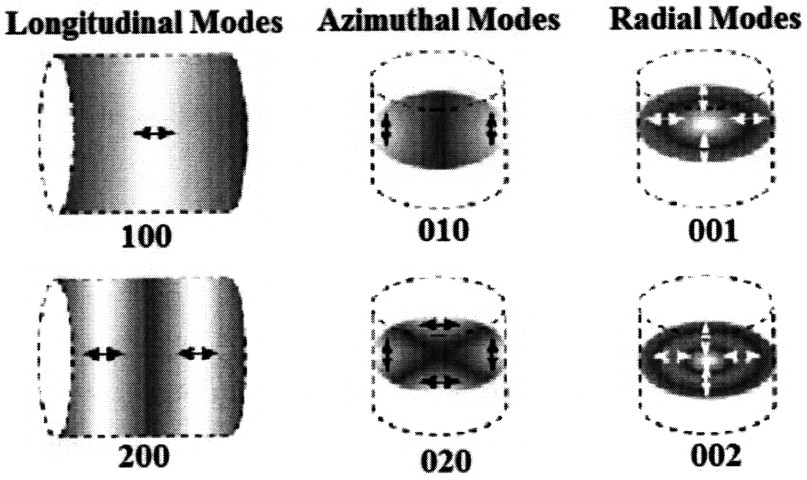

Figure 1-2: Illustration of pressure modes [1].

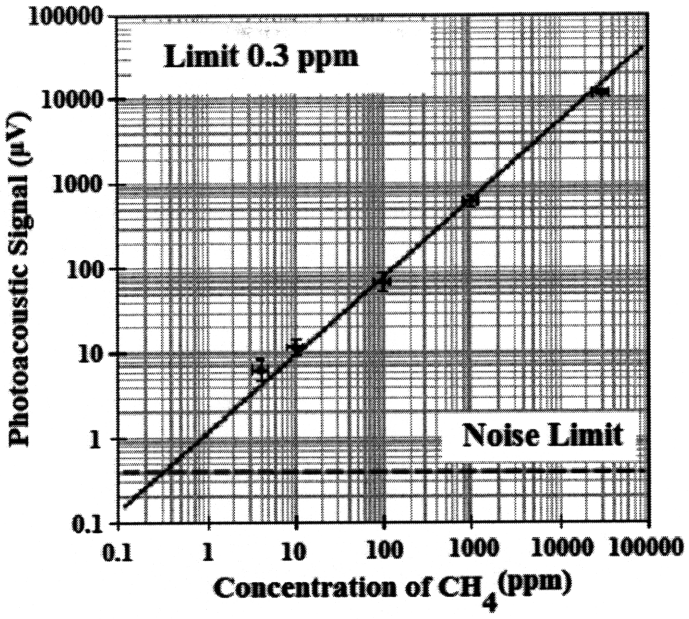

Figure 1-3: Experimental results showing linearity between CH_4 concentration and PA signal [12].

where V_c is the volume of the cylinder. This expression reveals that the pressure is directly proportional to the concentration of the gas and the length of the cavity L, and inversely proportional to the driving frequency ω and the cross-sectional area of the cavity (L/V_c). This linear relationship between the gas concentration and the pressure is observed in practice. An experimental plot of the concentration dependence of the voltage signal output from a pressure transducer is shown in Figure 1.3. Clearly, the linearity between sample concentration and PAS signal requires a linear relationship between other parameters in the PAS process (i.e., between transducer signal and pressure amplitude). This will be addressed in the following chapters.

Chapter 2

Laser Characterization and Radiation Modulation

2.1 Laser Characterization

The laser used was a 1558 nm DWDM direct modulation laser. The laser output was coupled through a built-in optical isolator into a single-mode fiber pigtail. Laser output power and central wavelength were found to vary as a function of the driving current and temperature of the laser medium. In order to fully characterize these relationships, wavelength and power were measured while sweeping temperature and current. Wavelength was measured using a Yokogawa Optical Spectrum Analyzer (OSA), and power was measured using a Hewlett Packard Power Meter. The results show that the wavelength and power are both linearly related to temperature and current.

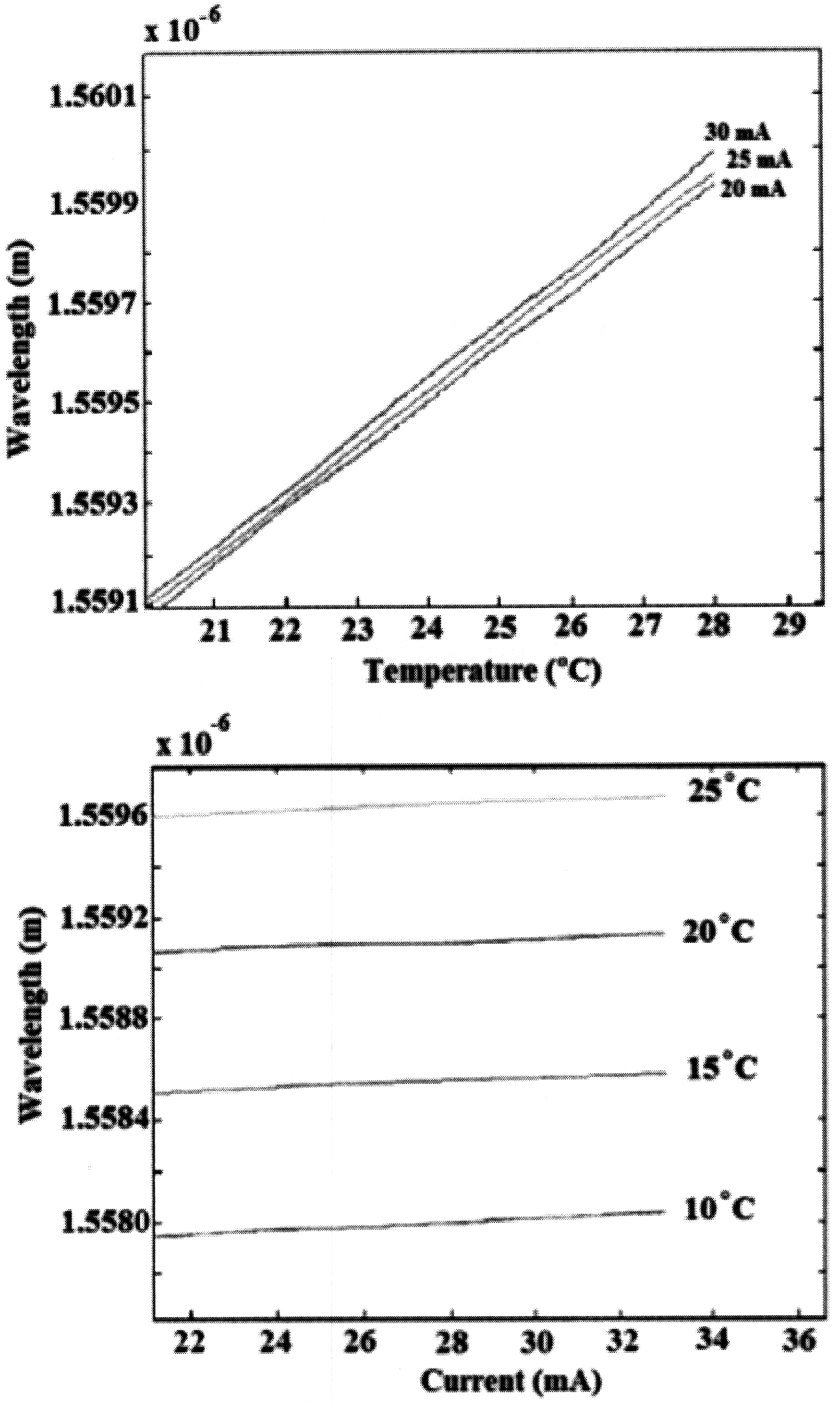

Figure 2-1: 1.55 μm laser wavelength characterization plots.

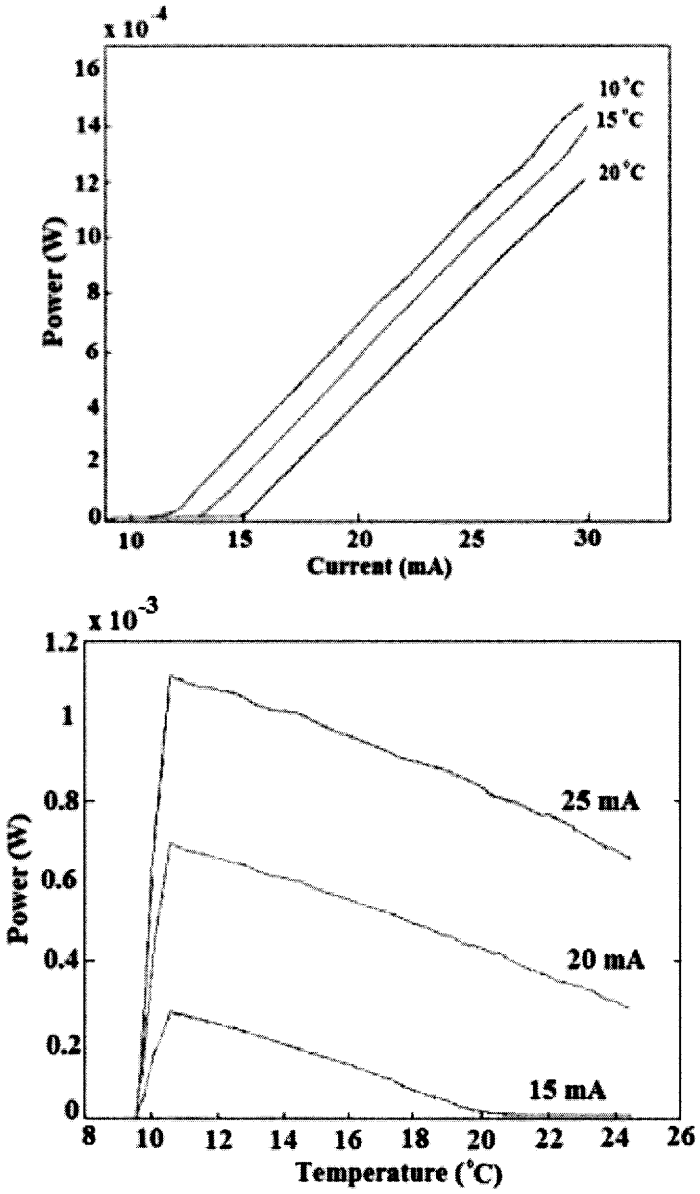

Figure 2-2: 1.55 μm power characterization plots.

Verification of the temperature vs. wavelength results from the OSA were done using a NIST reference absorption spectrum [17]. The calibration setup is shown below.

Laser output was split using a 3 dB coupler, whose mismatch factor was found to be negligible. One end was fed directly into a power meter, while the second end was coupled to a collimating lens, followed by a sample and a second power meter. $H^{13}C^{14}N$ at 100 Torr was found to be an appropriate choice of sample, as it absorbs

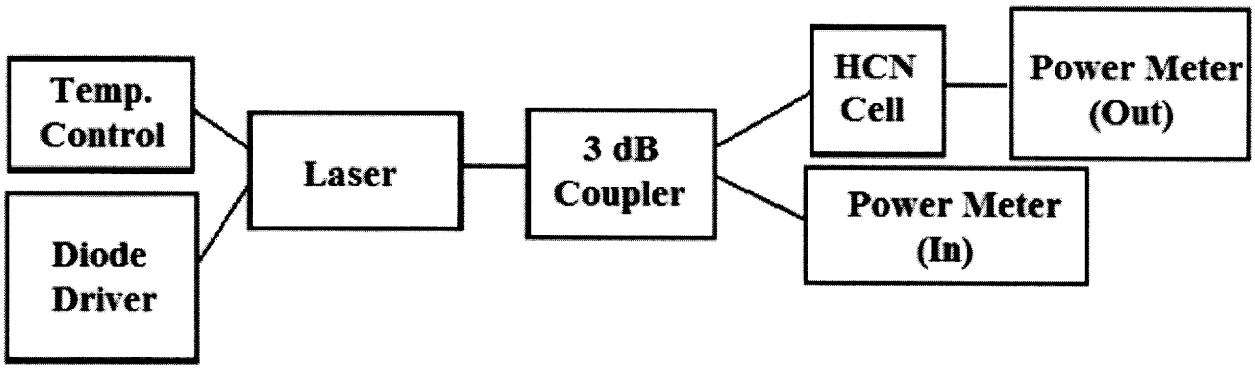

Figure 2-3: Calibration setup for absorption spectroscopy of 100 Torr HCN.

wavelengths between 1530 and 1560 nm. The absorbance A, or fraction of power absorbed by a sample, is given by:

$$A = 1 - \frac{P_{out}}{P_{in}} \tag{2.1}$$

Output power from the two ends of the fiber was measured as temperature was swept. Current was kept at 25 mA, while temperature was swept between 9° C and 30° C with steps of 0.05° C. The reference and experimental lines and their equivalent temperatures from three trials are listed in Table 2.1. The reference and experimental spectra are shown below. A new temperature-wavelength line was generated by using an average of the experimental temperatures and the reference wavelengths.

Reference	Trial 1 (° C)	(nm)	Trial 2 (° C)	(nm)	Trial 3 (° C)	(nm)
1558.033	9.90	1558.027	9.95	1558.032(5)	10.00	1558.038
1558.919	18.00	1558.912	18.15	1558.928	18.05	1558.917
1559.814	26.25	1559.812	26.20	1559.807	26.25	1559.812
1560.7185(6)	34.55	1560.719	34.55	1560.719	34.55	1560.719

Table 2.1: Reference [17] and Experimental Absorption Lines

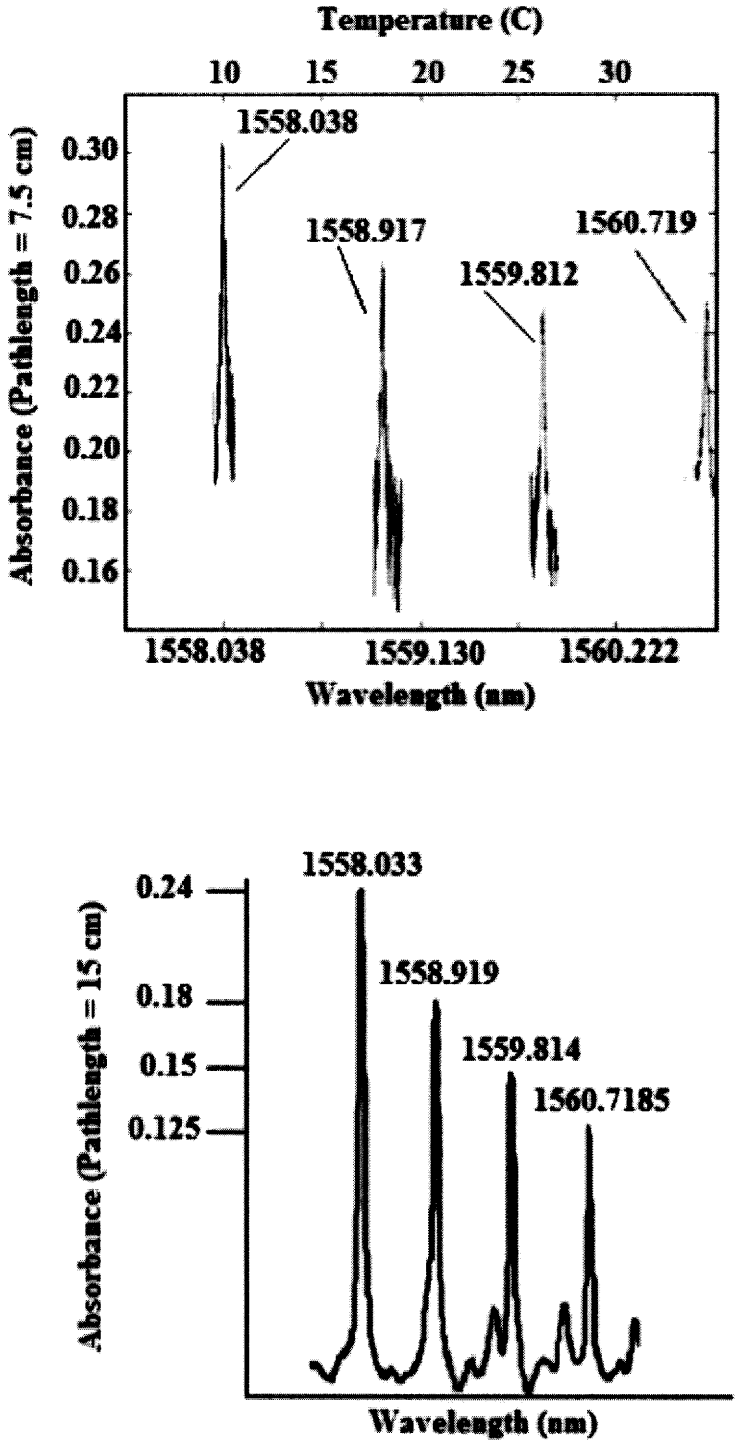

Figure 2-4: Experimental and reference [17] spectra for HCN.

Next, laser temperature was kept constant at each of the peak temperatures, while current was swept between 20 mA and 30 mA, with steps of 0.01 mA. The absorption coefficient α for the 1558.033 line was calculated from the absorption spectrum. It is known that the output power as a function of wavelength is given by the Beer-Lambert law:

$$P_{out} = P_{in}e^{-\alpha L} \tag{2.2}$$

where L is the length of the absorbing medium. Figure 2-5 shows the absorption coefficient, α, which was fit using two Lorentzians, one to the left and one to the right of 1558.0345 nm. The asymmetry in the curve is most likely due to the presence of another absorption peak to the left of the 1558.033 nm line. The model used was

$$\alpha(\lambda) = 0.01186 + \frac{5.73 \cdot 10^{-7}}{(\lambda - 1558.0345)^2 + 0.00925^2}, \ \lambda < 1558.0345 \tag{2.3}$$

$$\alpha(\lambda) = 0.00902 + \frac{1.49 \cdot 10^{-6}}{(\lambda - 1558.0345)^2 + 0.0125^2}, \ \lambda > 1558.0345 \tag{2.4}$$

where α is in cm^{-1}.

2.2 Current Modulation

The setup for wavelength modulation is shown in Figure 2-3. By knowing the current modulation waveform, the output power as a function of time can be predicted. The sinusoidal current modulation is of the form

$$I(t) = I_0 + \Delta I sin(\omega t) \tag{2.5}$$

where $I(t)$ is the instantaneous current, I_0 is the average current, ΔI is the current modulation depth, and ω is the modulation frequency. If the linear relationship between the laser wavelength and driving current is

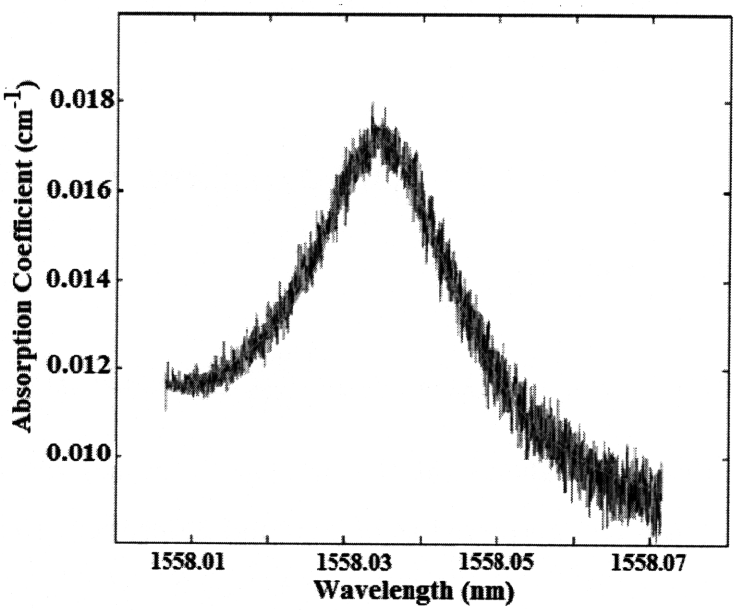

Figure 2-5: Absorption coefficient for the 1558.033 nm peak.

$$\lambda(I) = \lambda_0 + m_I I \tag{2.6}$$

where $\lambda(I)$ is the instantaneous laser wavelength and m_I is the slope of the current-wavelength line, then the wavelength modulation as a function of time is

$$\lambda(t) = \lambda_1 + \Delta\lambda sin(\omega t) \tag{2.7}$$

where,

$$\lambda_1 = m_I I_0 + \lambda_0 \tag{2.8}$$

$$\lambda = m_I \Delta I. \tag{2.9}$$

If we assume that αL is small, then using the Taylor expansion of e^x,

$$e^{-\alpha L} \approx 1 - \alpha L. \tag{2.10}$$

In the case of wavelength modulation, that is, $P_{in} = P_0$ and $\lambda(t)$ is prescribed by Eq. 2.7, output power from the sample is

$$P_{out} = P_0(1 - \alpha(\lambda_1 + \Delta\lambda sin(\omega t))L). \tag{2.11}$$

Expanding $\alpha(\lambda(t))$ for small $\Delta\lambda$,

$$\alpha(\lambda(t)) = \alpha_0 + \frac{\partial\alpha}{\partial\lambda}\Delta\lambda sin(\omega t) + \frac{1}{2}\frac{\partial^2\alpha}{\partial\lambda^2}(\Delta\lambda)^2 sin^2(\omega t) + ..., \tag{2.12}$$

where the derivatives are evaluated at the wavelength around which modulation is performed, and α_0 can be interpreted as background absorption. Now,

$$P_{out} = P_0(1 - L[\alpha_0 + \frac{\partial\alpha}{\partial\lambda}\Delta\lambda sin(\omega t) + \frac{1}{2}\frac{\partial^2\alpha}{\partial\lambda^2}(\Delta\lambda)^2 sin^2(\omega t) + ...]) \tag{2.13}$$

From this equation, it can be seen that the contribution to the ω harmonic is proportional to $\frac{\partial\alpha}{\partial\lambda}$. Using the trigonomentric identity $sin^2(\omega t) = \frac{1}{2} - \frac{1}{2}cos(2\omega t)$, we can see that the 2ω harmonic is proportional to $\frac{\partial^2\alpha}{\partial\lambda^2}$.

However, the laser being used modulates both amplitude (power) and wavelength simultaneously, thus, assuming that $P_{in} = P_0 + \Delta P sin(\omega t)$,

$$P_{out} = (P_0+\Delta P sin(\omega t))(1-L[\alpha_0+\frac{\partial\alpha}{\partial\lambda}\Delta\lambda sin(\omega t)+\frac{1}{2}\frac{\partial^2\alpha}{\partial\lambda^2}(\Delta\lambda)^2 sin^2(\omega t)+...]). \tag{2.14}$$

This result reveals that α_0, or background absorption, contributes to the ω signal, whereas it does not contribute to the 2ω signal. Thus, to avoid the effects of background absorption, a strong 2ω signal and a weak ω signal should be used for PAS.

Additionally, since the expansion of α in Eq. 2.12 is an infinite series, we should expect P_{out} to consist of an infinite number of harmonics. The plot in Figure 2-6 shows this. It was generated with a numerical model using the α fit in Eqs. 2.3 and 2.4. In the model, absorbance was modulated as a function of time using the power and wavelength modulation prescribed above with the values of modulation depth and amplitude equivalent to those in the experiment that will be described next.

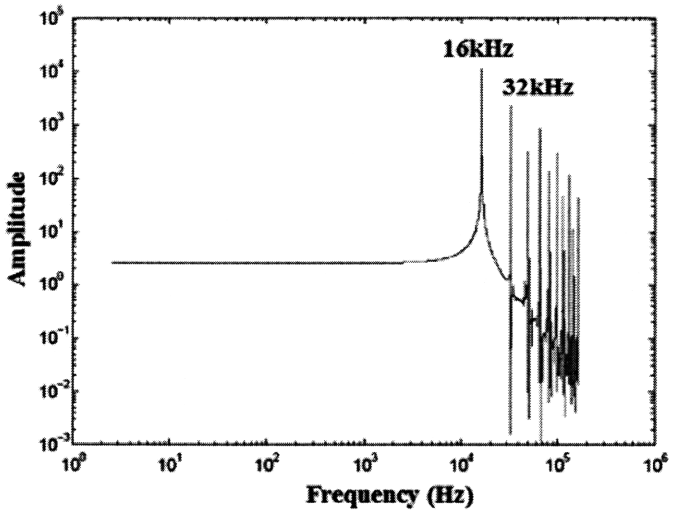

Figure 2-6: FFT of P_{out}, illustrating an infinite number of harmonics.

Since the lowest step size for either current modulation or temperature modulation is 0.01 mA or 0.01 C, Figure 2-1 shows that finer resolution can be achieved by using current modulation. For instance, for a 0.01 step size in current, a step size of 3.59e-5 nm in wavelength can be achieved, whereas a 0.01 step size in temperature would give 1.09e-3 nm. In addition, current modulation is preferred over temperature modulation, since changes in temperature are not as instantaneous as with changes in current.

The following results were generated by wavelength modulation around the 1558.033 peak. The current modulation depth was 6.15 mA, which equated to a wavelength modulation of 0.025 nm. This line was initially chosen simply due to its strength. Typically, however, line selection is an important process. When doing PAS on a gas that is a constituent of a mixture of several species, the line around which to modulate must be chosen such that it is isolated from lines of competing species.

As was discussed previously, it was necessary to determine how to generate a strong 2ω and weak ω signal. To determine this, the ideal wavelength around which to modulate was found by varying the temperature and keeping the current constant. Figure 2-7 shows the theoretical amplitudes of the first and second harmonics and their ratio as a function of temperature and their equivalent wavelengths for a mod-

ulation frequency of 16 kHz and a wavelength modulation depth of 0.025 nm (6.15 mA).

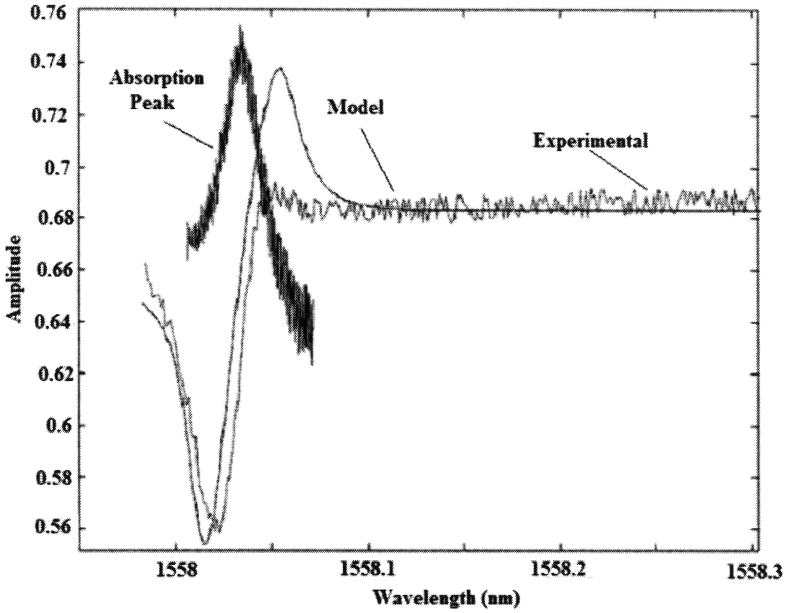

Figure 2-7: Amplitude of the experimental and theoretical first harmonic, showing its relation to the first derivative of the absorption spectrum.

From the plots, it appears that the amplitude of the 16-kHz harmonic is related to the first derivative of the absorption spectrum, and the amplitude of the 32-kHz harmonic is related to the second derivative. Thus, these observations confirm the results from above.

Given that the temperature sweep revealed that current modulation around 1558.033 nm would give the highest ratio between the 32-kHz and 16-kHz harmonics, the next step was to determine the ideal modulation width. This was done three ways, analytically and numerically. In the numerical model, modulation depth was swept between 0 and 7 mA with steps of 0.01 mA, while the amplitudes of the 32-kHz and 16-kHz harmonics were measured. A plot of the results are shown below in Figure 2-9. Analytically, if we assume that the absorption coefficient alpha goes as:

$$\alpha = \frac{\eta}{\kappa(\lambda - \lambda_0)^2 + \xi^2} \tag{2.15}$$

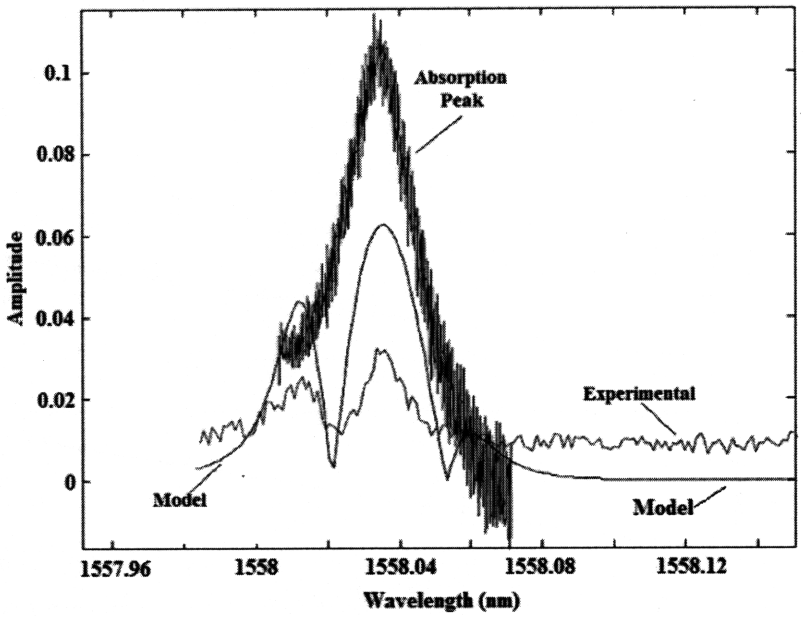

Figure 2-8: Amplitude of the experimental and theoretical second harmonic, showing its relation to the second derivative of the absorption spectrum.

where η, κ, and ξ are constants, then

$$\frac{d\alpha}{d\lambda} = \frac{-2\eta\kappa(\lambda - \lambda_0)}{[\kappa(\lambda - \lambda_0)^2 + \xi^2]^{-2}} \tag{2.16}$$

$$\frac{d^2\alpha}{d\lambda^2} = \frac{2\eta\kappa(4\kappa(\lambda - \lambda_0)^2 - \kappa(\lambda - \lambda_0)^2 - \xi^2)}{[\kappa(\lambda - \lambda_0)^2 + \xi^2]^3} \tag{2.17}$$

Inserting $\lambda = \Delta\lambda sin(\omega t)$,

$$\frac{\frac{d^2\alpha}{d\lambda^2}}{\frac{d\alpha}{d\lambda}} = \frac{3\kappa(\Delta\lambda)^2 sin^2(\omega t) + \xi^2}{[\kappa(\Delta\lambda)^2 sin^2(\omega t) + \xi^2]\Delta\lambda sin(\omega t)} \tag{2.18}$$

which can be approximated as

$$\frac{3\kappa(\Delta\lambda)^2 + \xi^2}{\kappa(\Delta\lambda)^3 + \xi^2(\Delta\lambda)} \tag{2.19}$$

The behavior of this result matches that from the numerical results. These results clearly indicate that the lower the modulation depth, the higher the $2f$ to f ratio. However, as the modulation depth decreases, so does the amplitude of the $2f$ har-

monic, thus in choosing an optimal modulation depth, both the ratio of the $2f$ to f harmonics as well as the noise levels in comparison to the amplitude of the $2f$ harmonic should be taken into account.

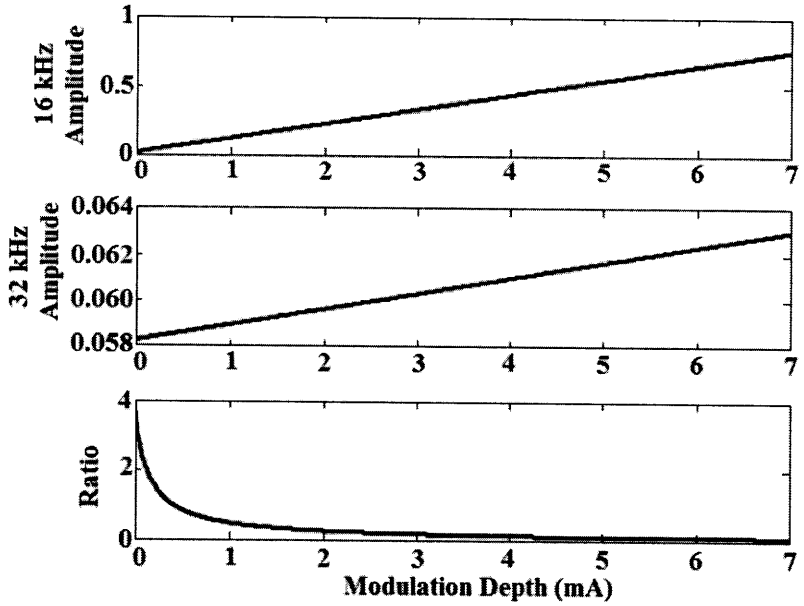

Figure 2-9: Numerical model showing the behavior of the first two harmonics and the ratio of the 2nd to 1st harmonic as a function of modulation depth.

2.2.1 Amplitude Vs. Frequency Modulation Revisted

As was indicated before, both frequency and amplitude modulation may be used in PAS, however the former is more advantageous when background absorption is present in the sample. It is clear that both methods create time-varying output power signals:

$$P_{out} = (P_0 + \Delta P sin(\omega t))e^{-\alpha L} \tag{2.20}$$

for amplitude modulation, and

$$P_{out} = P_{in}e^{-\alpha(t)L}. \tag{2.21}$$

for wavelength modulation. Assuming, however, that absorption as a function of λ consists of two sources, a background absorption equal to a constant X, plus a peak (see Figure 2-10) Y(λ), then in the case of amplitude modulation, the absorbance A is

$$\begin{aligned} A &= X + Y(\lambda) \\ &= 1 - \frac{P_{out}}{P_{in}} \end{aligned}$$

thus,

$$\begin{aligned} P_{out}(\lambda) &= P_{in}(1 - X - Y(\lambda)) \\ &= [P_0 + \Delta P sin(\omega t)](1 - X - Y) \\ &= P_{in} - P_{in}X - P_{in}Y(\lambda) \end{aligned} \tag{2.22}$$

In the case of a small weak peak absorance and strong background signal, such that X >> Y, then the third term in Eq. 2.20 is drowned out. On the other hand, for wavelength modulation, for which

$$\begin{aligned} P_{out} &= P_{in}(1 - X - Y(\lambda(t))) \\ &= P_{in} - P_{in}X - P_{in}Y(\lambda(t)) \end{aligned} \tag{2.23}$$

the second term acts as a DC signal, and the third term is the desired modulated peak signal. This is highly advantageous in the case where the background signal is strong, and the peak signal is weak. The background signal never drowns out the peak signal, as was the case with amplitude modulation.

From the analysis of radiation modulation, it is clear that in order to achieve large PAS signals with the second harmonic, wavelength modulation must be used,

and the modulation depth must be small. In addition, the wavelength around which to modulate and the modulation depth must be chosen so as to not only maximize the second harmonic, but to also minimize the ratio of the first to second harmonics.

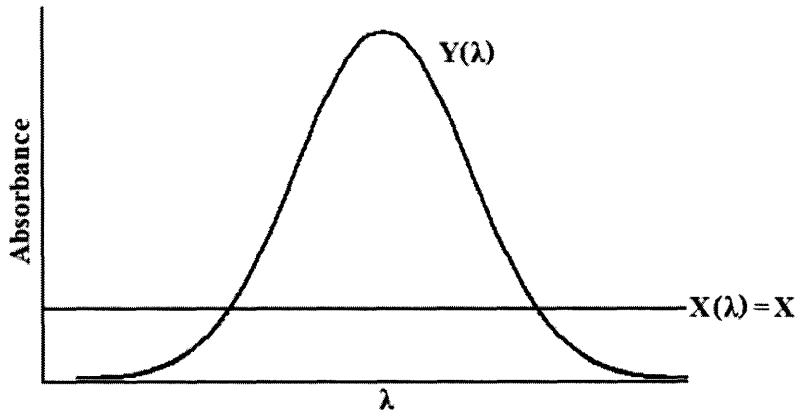

Figure 2-10: Sketch of background absorption approximated as a contant X, and an absorption peak Y(λ).

Chapter 3

Tuning Fork Characterization

3.1 Theory

This section discusses the third part of the PAS process: the pressure transducer. In QEPAS, a quartz-crystal tuning fork is used instead of a microphone.

Piezoelectricity is the coupling between internal dielectric polarization and strain, and is present in most crystals lacking a center of inversion symmetry. When a stress is applied to these materials, it induces a displacement of charge and a net electric field. The effect is reversible; when a voltage is applied across a piezoelectric material, it is accompanied by a strain. To give a sense of the scale of these forces, if a 1000 V/m electric field is applied along a rod of quartz, the resulting strain is on the order of 10^{-7} N. Conversely, large mechanical forces induce small electric fields. The direction in which these strains occur depends on its stiffness, compliance, and piezoelectric coefficients, which are third-rank tensors. The displacement vector is related to the stress induced by [22]:

$$D = dS + \varepsilon E \tag{3.1}$$

where D is the displacement vector in C/m^{-2}, d is the piezoelectric coefficient matrix in C/N, S is the stress vector in N/m^{-2}, and ε is the permittivity matrix. In matrix form, Eq. 3.1 becomes

$$\begin{bmatrix} D_1 \\ D_2 \\ D_3 \end{bmatrix} = \begin{bmatrix} d_{11} & -d_{11} & 0 & d_{14} & 0 & 0 \\ 0 & 0 & 0 & 0 & -d_{14} & -2d_{11} \\ 0 & 0 & 0 & 0 & 0 & 0 \end{bmatrix} \begin{bmatrix} S_1 \\ S_2 \\ S_3 \\ S_4 \\ S_5 \\ S_6 \end{bmatrix} + \begin{bmatrix} \varepsilon_{11} & \varepsilon_{12} & \varepsilon_{13} \\ \varepsilon_{21} & \varepsilon_{22} & \varepsilon_{23} \\ \varepsilon_{31} & \varepsilon_{32} & \varepsilon_{33} \end{bmatrix} \begin{bmatrix} E_1 \\ E_2 \\ E_3 \end{bmatrix}$$

where the piezoelectric coefficients have been replaced with those for quartz. The strain on the material is [22]

$$s = CS + dE \tag{3.2}$$

where s is the strain vector, C is the compliance matrix in m^2/N, and E is the electric field vector in V/m. This equation in matrix form becomes:

$$\begin{bmatrix} s_1 \\ s_2 \\ s_3 \\ s_4 \\ s_5 \\ s_6 \end{bmatrix} = \begin{bmatrix} C_{11} & C_{12} & C_{13} & C_{14} & 0 & 0 \\ C_{12} & C_{11} & C_{13} & -C_{14} & 0 & 0 \\ C_{13} & C_{13} & C_{33} & 0 & 0 & 0 \\ C_{14} & -C_{14} & 0 & C_{44} & 0 & 0 \\ 0 & 0 & 0 & 0 & C_{44} & C_{14} \\ 0 & 0 & 0 & 0 & C_{14} & (C_{11} - C_{12})/2 \end{bmatrix} \begin{bmatrix} S_1 \\ S_2 \\ S_3 \\ S_4 \\ S_5 \\ S_6 \end{bmatrix} +$$

$$+ \begin{bmatrix} d_{11} & -d_{11} & 0 & d_{14} & 0 & 0 \\ 0 & 0 & 0 & 0 & -d_{14} & -2d_{11} \\ 0 & 0 & 0 & 0 & 0 & 0 \end{bmatrix} \begin{bmatrix} E_1 \\ E_2 \\ E_3 \end{bmatrix}$$

where the compliance coefficients have been replaced with those for quartz. Due to this intrinsic coupling of strain and charge displacement, the tuning fork can be modelled both electrically and mechanically. To see this, each prong of the tuning fork can be modelled as a slab of dimensions H x L x W.

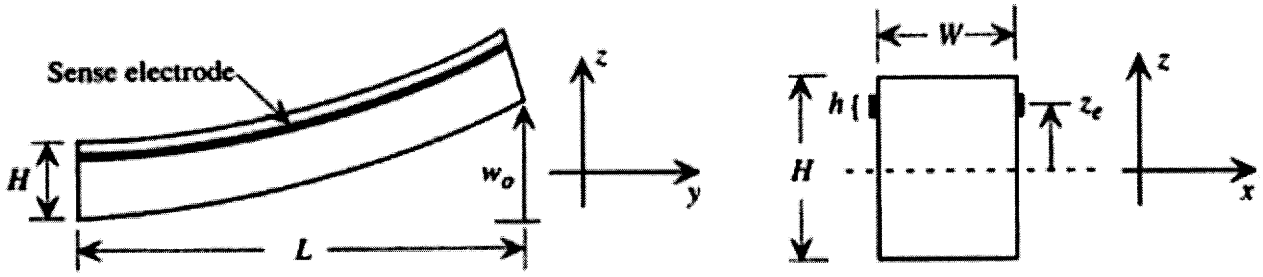

Figure 3-1: Diagram of a tuning fork tine [22].

Due to the structure of its tensors, if an electric field is applied in the x-direction of the quartz slab, it will result in a bending motion in the z-direction. Both this mechanical motion and electrical behavior can be modelled as differential equations, which take on equivalent forms. Thus, the tuning fork is both a circuit with capacitance C, resistance R, and inductance L, and equivalently a mass 'm' on a spring with spring constant 'k' and damping factor 'β'. Consequently, R, L and C each have mechanical counterparts, β, m, and 1/k, respectively. The two domains can be coupled through a transformer relation, in which the force driving the tuning fork is proportional to the driving voltage [22]:

$$F = m\frac{d^2x}{dt^2} + \beta\frac{dx}{dt} + kx \tag{3.3}$$

$$V = L\frac{d^2q}{dt^2} + R\frac{dq}{dt} + \frac{1}{C}q \tag{3.4}$$

$$F = nV,\ n = \frac{C_{11}d_{12}H^3}{6z_eL^2} \tag{3.5}$$

$$\tag{3.6}$$

Hence, a voltage signal measured from the tuning fork can easily be translated into the force (and therefore pressure) on it.

3.2 Characterization

The PAS transducer used in these experiments was an Abracon quartz tuning fork with a 12.5 pF load capacitance and a 32.768 kHz resonance frequency. The tuning fork came vaccuum sealed in a steel canister, which could be removed. The diagram of the tuning fork in the cannister is shown in Figure 3-2.

The circuit schematic used to characterize the fork is in Figure 3-3.

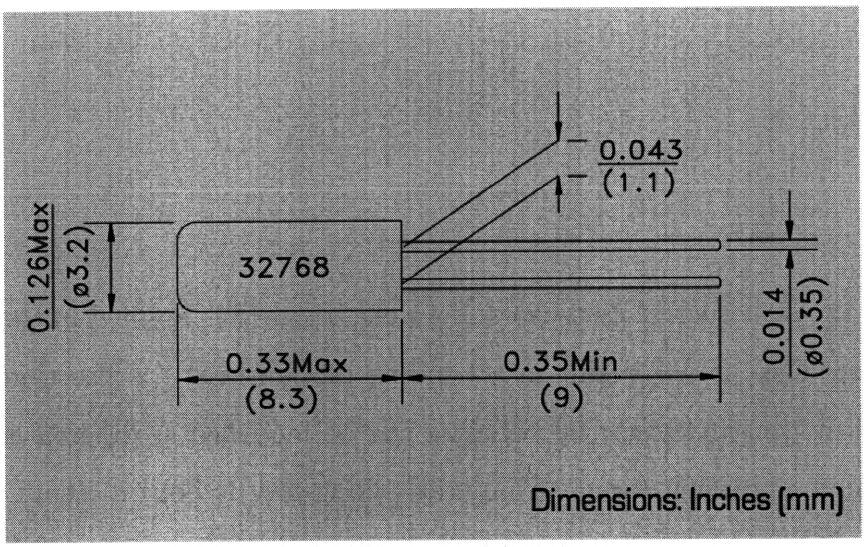

Figure 3-2: Diagram of tuning fork within canister from the Abracon datasheet.

A signal generator with a 50 Ω load resistance served as the voltage source to the tuning fork. The output from the circuit was fed to an A-to-D converter, which measured the amplitudes of the input and output voltages and their relative phases. Since the A-to-D converter possessed a saturation voltage of 9 V, a voltage divider was placed such that the input was guaranteed to reach the threshold.

The expected output voltage is:

$$V_{out} = \frac{R_f A'}{\mid Z(\omega) \mid}, \tag{3.7}$$

where A' is the voltage signal amplitude after passing through the voltage divider,

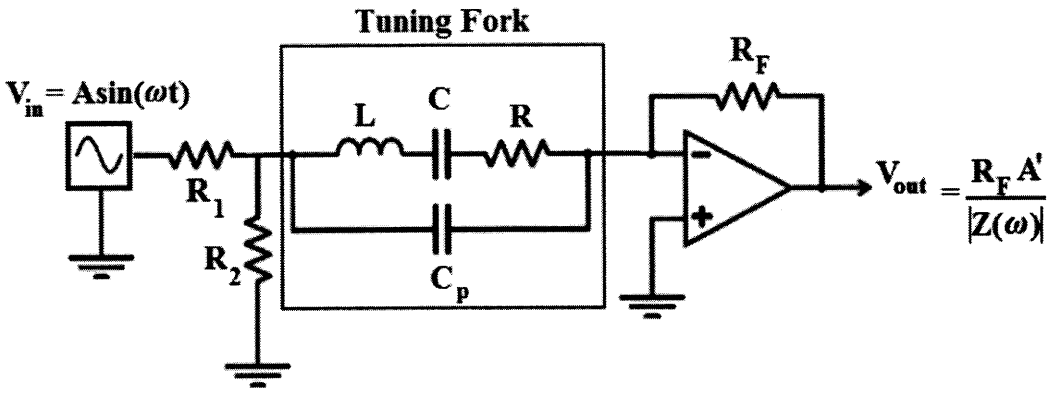

Figure 3-3: Schematic of circuit to characterize tuning fork.

and Z is the impedance of the tuning fork, given by:

$$Z(\omega) = \omega\left(\frac{jC}{-LC(\omega - \frac{jR}{2L})^2 + (1 - \frac{CR^2}{4L})} + jC_p\right) \tag{3.8}$$

The values for the inductance, capacitance and resistance were found experimentally by performing a frequency sweep while measuring output amplitude. As the effect of C_p was found to be negligible on the impedance, the tuning fork lumped-model was reduced to an RLC series circuit. Thus, the resonant frequency reduced to

$$\omega_0 = \frac{1}{\sqrt{LC}} \tag{3.9}$$

while the impedance at resonance was equal to its resistance.

An equivalent experiment was performed on the tuning fork with the canister removed. A frequency sweep showed that the value of the resonance frequency and the value of the amplitude both decreased. The decrease in amplitude can be attributed to the increase in resistance in the electrical model, and thus an increase in the damping factor in the mechanical model.

The change in resonant frequency indicates that the resonant frequency will have to be kept track of when performing spectroscopy on the various concentrations of a sample gas. However, since PAS is used for a relatively small range of extremely small concentrations, it can be assumed that the resistance to which the tuning fork

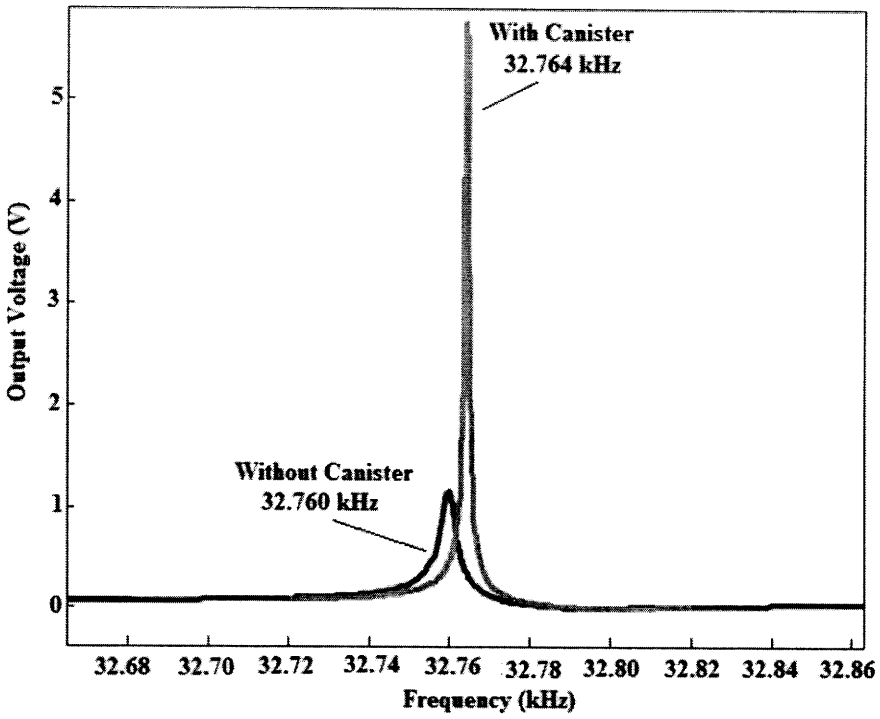

Figure 3-4: Frequency sweep of tuning fork, showing that the resonant frequency and amplitude at resonance decreases as damping decreases.

will be subjected to will not change appreciably over the concentration range.

3.3 Photoacoustic Signal vs. Sample Concentration

Ultimately the PAS signal is measured as a voltage signal from the tuning fork. Under the assumption that at sufficiently low concentrations, a change in sample concentration causes negligible change in absorption linewidth, it can be shown that the PAS signal will be linear as a function of sample concentration:

- Using Eqs. 1.3 and 2.13, the second harmonic of P_{out} is proportional to the concentration N.
- Eq. 1.15 shows that the pressure amplitude is linear with α and hence sample concentration.

- Eq. 3.7 shows that the output voltage signal from the tuning fork is proportional to driving voltage, which is in turn proportional to the driving force, and thus also to the pressure amplitude.

Chapter 4

QEPAS of NH_3

NH_3 is a colorless gas with a distinct odor and occurs both naturally and as a result of human activity. There has been an increasing interest in the spectroscopy of NH_3, due its important role in the environment, in agriculture, and as a disease biomarker. In particular, the medical field has gained increasing interest in its detection, because it is a biomarker of respiratory diseases. Ammonia is also used in animal production facilities, emitted by traffic, and used to reduce NOx emissions in factories. In addition, it plays an important role in balancing in the ecosystem, as its overabundance in nature can cause acidification and eutrophication of the environment [2]. The main source of NH_3 is from agriculture, followed by other industries, namely household products. Agricultural sources include animal waste (cattle, pigs, sheep), and the use of fertilizers (ammonium sulphate, ammonium nitrate, ammonia, urea and ammonium phosphate). Before 1995, ammonia emissions from traffic were considered negligible, until car companies started widely utilizing catalytic converters, which convert NO and H to NH_3 to reduce emission of more dangerous pollutants.

4.1 Characterization of 1.53 μm Laser

The ammonia molecule possesses strong lines in the 1.53 μm region. In the region 1450 to 1560 nm, Lundsberg-Nielsen *et al* [9] have identified 1710 ammonia absorption lines, assigning 381 to rotation-vibrational transitions. Thus, a 1.53 μm DFB laser

was used for ammonia spectroscopy. A temperature sweep and current sweep were performed on the laser to determine the dependence of wavelength and power on temperature and current. The results are shown in Figure 4-1.

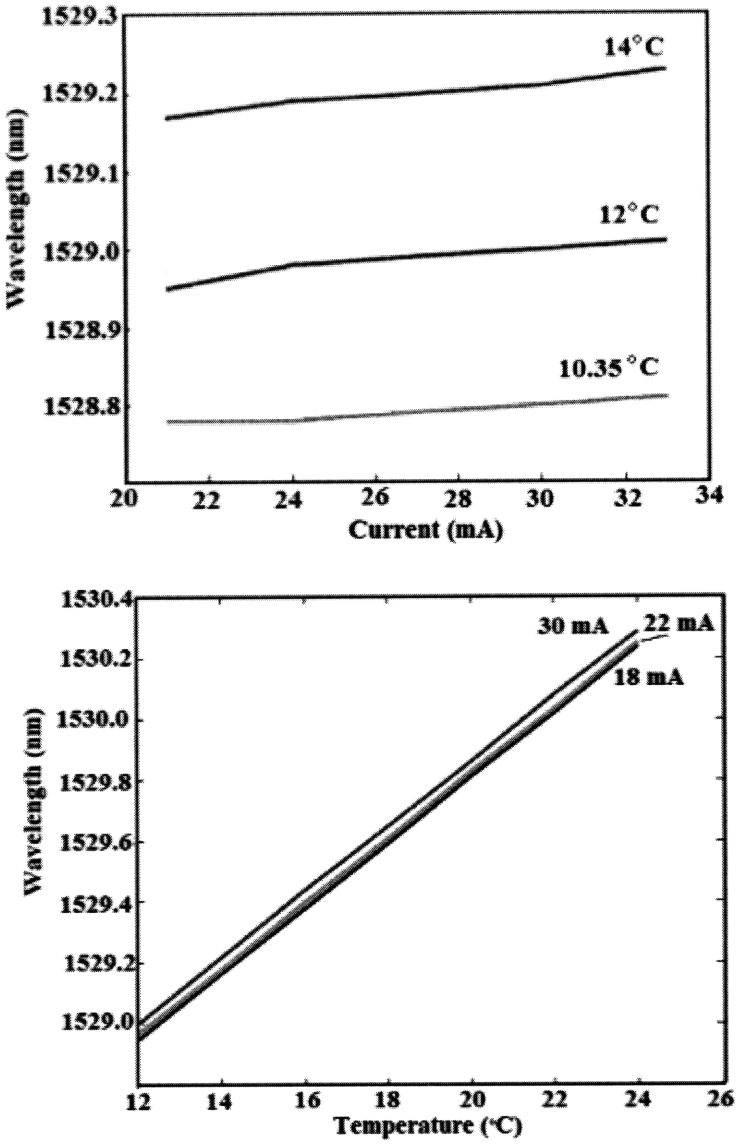

Figure 4-1: 1.53 μm laser wavelength characterization plots.

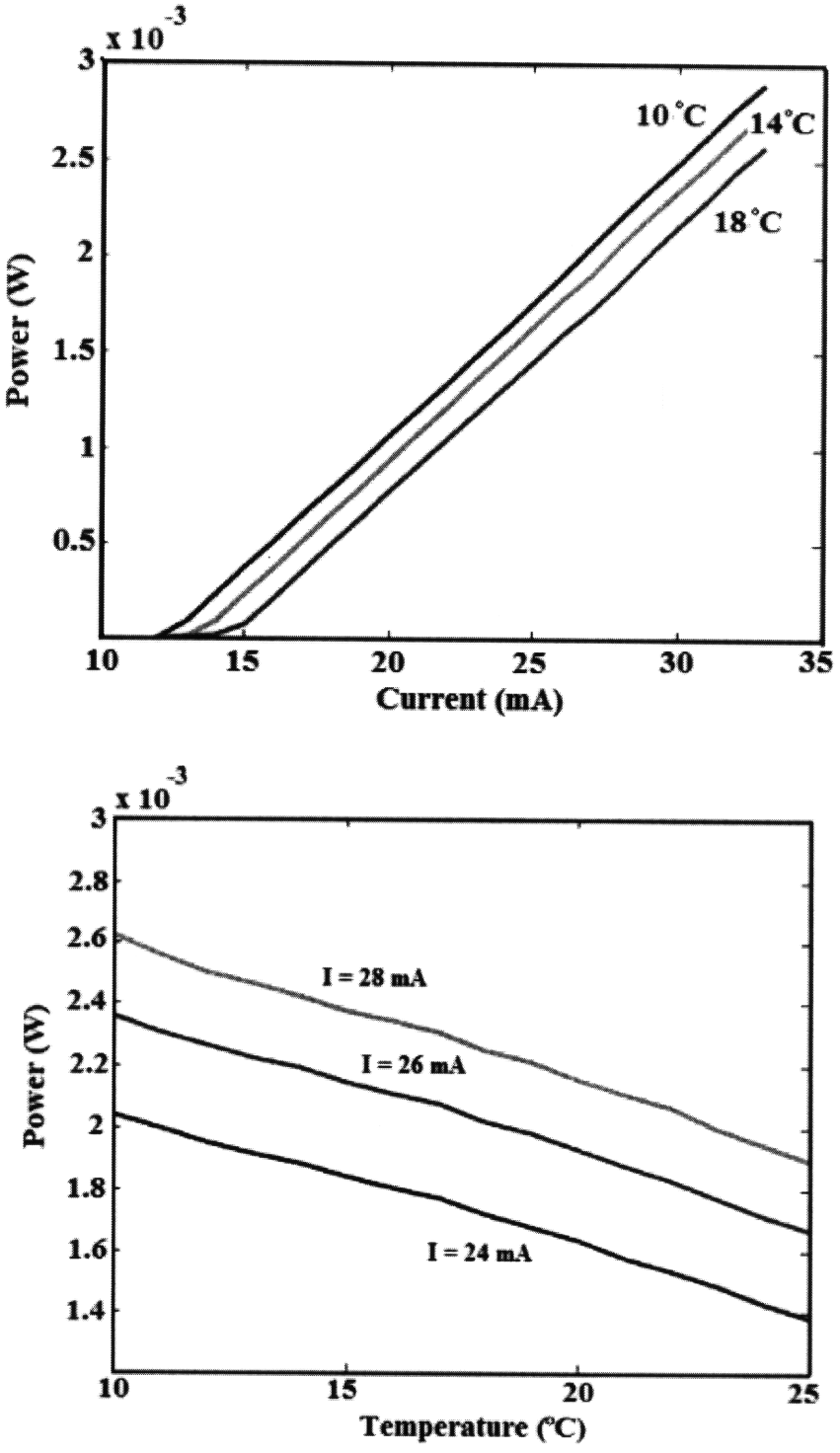

Figure 4-2: 1.53 μm laser output power characterization plots

The behavior of these plots follows that of 1.55 μm laser, with the exception of the wavelength vs. power plot. It is not known what the cause of this behavior is, and it will have to be pursued further in order to perform radiation modulation.

4.2 NH_3 Spectrum

The same setup as in Figure 2.3 was used to perform absorption spectroscopy on a 100 Torr NH_3 sample. The experimental results are shown in Figure 4.3. The temperature sweep resolved only six peaks, at 1528.713, 1528.793, 1529.569, 1529.827, 1530.307, and 1530.588 nm, and there was difficulty in determining where overlapping between lines occurred.

To verify the lines, the results were compared to a reference spectrum [9]. The decision over which line to choose for wavelength modulation was dependent on line isolation, line strength, and laser temperature threshold. Clearly, the 1530.588 nm is a composite of two strong lines, and the 1528.713 nm line is too close to the minimum temperature, thus the 1529.827 line was chosen for measurement.

4.3 Generating NH_3

Due to its prevalence in many industries, much research has been done on the generation of ammonia, and there are several well-known procedures. On the industrial scale, the Haber process is used [2] by reacting nitrogen gas with hydrogen gas, but this method is not appropriate for purposes on a small scale. A second method is the well-known Ammonia Fountain, which utilizes NaOH and NH_4Cl crystals, which are mixed in a flask with H_2O. The reaction in the flask is

$$NH_4 + NaOH \rightleftharpoons NH_3 + H_2O + Na^+ + Cl^- \tag{4.1}$$

The vapor contents flow through a dessicant such as anhydrous $CaS0_4$ and then through a tube of NaOH to filter out any remaining water vapor. The NH_3 is then collected in a second beaker [19].

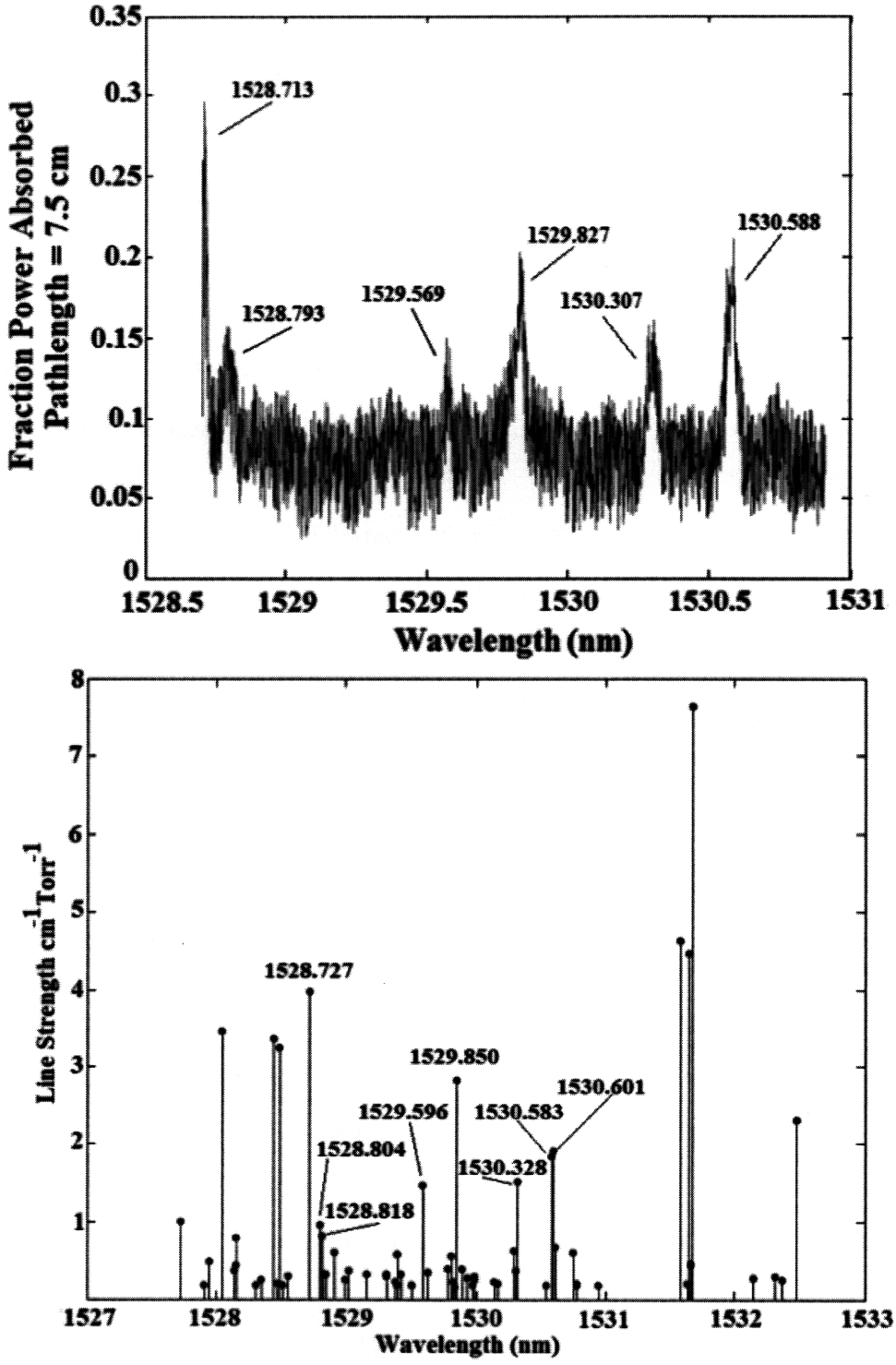

Figure 4-3: Experimental and reference [9] Absorption Spectrum of NH_3

The simplest method of generating NH_3, however, involves taking advantage of the low vapor pressure of ammonium hydroxide. Solutions with less than 40

Household ammonium hydroxide was initially chosen, as it typically contains between 5 and 10% percent ammonia by weight. According to basic physical chemistry, when the solution is in equilibrium, most of the ammonia is dissolved in water as NH_4^+, but a trace amount remains as NH_3 vapor. This can be quantified by calculating the equilibrium reaction constant K_{eq}:

$$K_{eq} = \frac{[NH_3][H_20]}{[NH_4^+][OH^-]} \tag{4.2}$$

The constant K_{eq} is related to the Gibbs Free Energy through the expression

$$\Delta G = -RTlnK \tag{4.3}$$

The thermodynamic requirement for a decrease in Gibbs free energy means that K_{eq} must be positive, so there will always be some ammonia vapor in equilibrium with the solution. For the same reasons, water vapor must also be in equilibrium with the liquid. However, since water vapor does not have absorption lines in the region of 1.53 μm, ammonium hydroxide was an appropriate choice. This was verified by performing spectroscopy of air at room pressure, which revealed negligible absorption at the laser's wavelengths. In addition, the presence of water vapor is advantageous, since PAS works best when the sample is accompanied by noncompeting species at higher pressures [4],

Two methods of creating an NH_3 were used. The first involved the setup for making "homemade ammonia" in Figure 4-4. The system used brass and steel valves and Swageloks, and a beaker to serve as a 'reservoir' of ammonium hydroxide. First stiffer piping was used to connect the elements, but it was found to promote leakage, so PVC piping was ultimately used.

The following steps were followed to create samples of ammonia: 1.) valve 1 was kept closed as valve 2 and the needle valve were left open, while vacuum 1 pumped out air in the beaker, 2.) valve 2 and the needle valve were then closed as vacuum

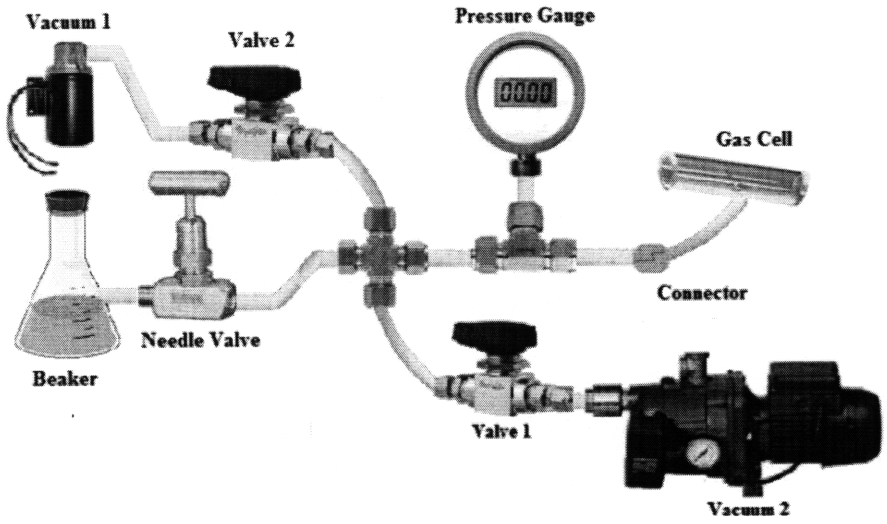

Figure 4-4: Setup for making NH_3.

2 pulled contaminants from the gas cell, 3.) then valve 1 was then closed, and then needle valve opened to let ammonia into the gas cell, 4.) the tubing attached to the gas cell was then clamped and disconnected from the system for spectral analysis.

The majority of the first batch of samples showed no features reminiscent of absorption lines. It was deduced that the surfactant may have been a competing species, so a second method was used to "make" ammonia. A vial of 30% pure ammonium hydroxide was attached directly to the gas cell, and the contents within the cell were left to reach equilibrium. Figure 4-5 shows one of the more successful absorption spectra, revealing a weak 1530.588 nm line. The experiment was interrupted toward the latter part of the sweep, however, due to the movement of the gas cell, as it was not secured properly.

4.4 Tuning Fork Assembly

As a primary step toward generating photoacoustic signals, an assembly was fabricated (courtesy of Dr. Harry Lee). Three holes were drilled in a slab of polycarbonate, one in which to place the tuning fork (with the top of the canister removed), and two (holes A and B in Figure 4-6) to place in screws to keep the tuning fork in place. A

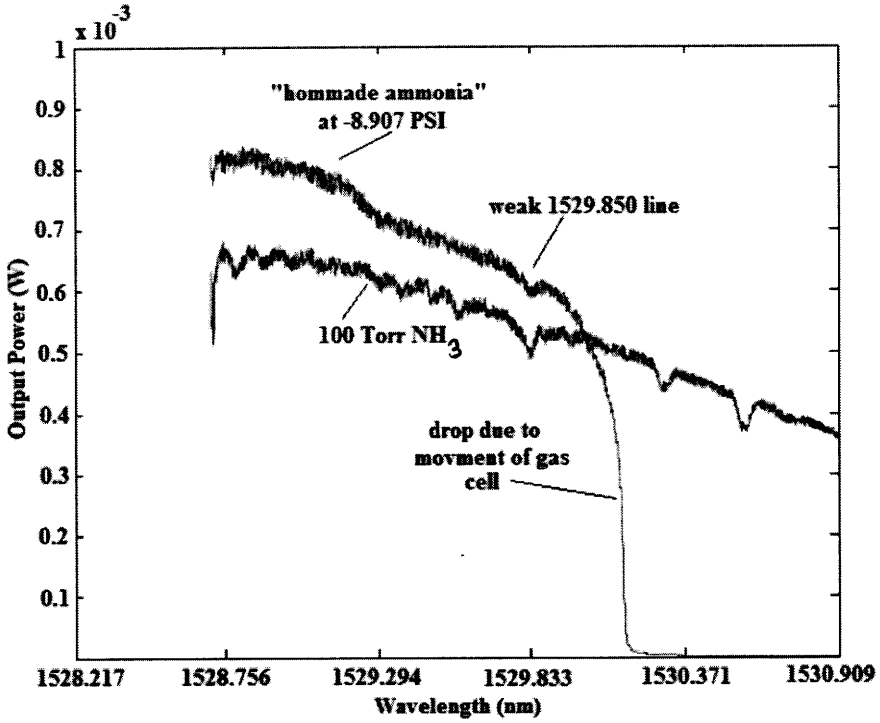

Figure 4-5: Vaccuum system setup for making NH_3.

v-groove was etched into the polycarbonate such that an optical fiber could be held in place. The fiber was placed so that the laser beam would be directed through the prongs of the tuning fork.

This assembly will eventually be held over a beaker (tuning-fork face-down) of ammonium hydroxide. The tuning fork will be connected to the circuit in Figure 3-3. The signal from the tuning fork will then be compared to that when the assembly is exposed to air only.

Ultimately, the concentration of ammonia will have to be known in order to generate a PAS signal vs. ammonia concentration curve, and thus the vapor-liquid equilibrium behavior of ammonium hydroxide will need to be fully understood if it is to be used as a source of NH_3.

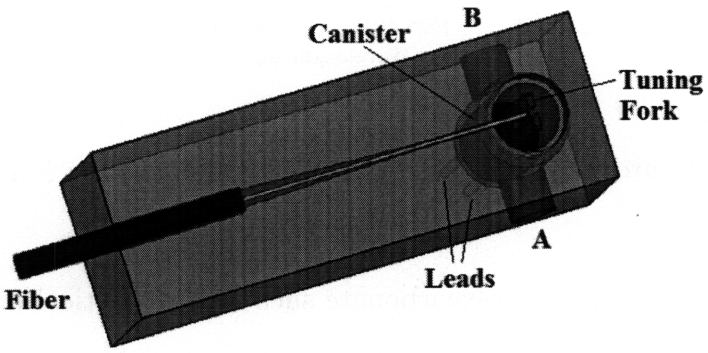

Figure 4-6: Tunking fork assembly [18]

Chapter 5

Conclusion

5.1 Summary of Results

The goals of this project were to analyze the processes of QEPAS analytically, numerically and experimentally. Although photoacoustic signals were not realized ultimately, the following results were found:

- Wavelength modulation is preferred over amplitude modulation, because the background absorption in the former method merely acts as a DC signal, whereas in the latter method, the background absorption is modulated and can drown out the peak signal. This is also one reason that PAS via wavelength modulation is more sensitive than absorption spectroscopy for trace sample concentrations.

- In sinusoidal wavelength modulation, the first and second harmonics are proportional to the first and second derivatives of the absorption peak, respectively.

- The quartz-crystal tuning fork is a convenient pressure transducer to utilize in QEPAS, because its voltage output is proportional to the force (and thus pressure) driving the tuning fork.

- Lastly, the QEPAS signal is linear with sample concentration for the reasons mentioned in Chapter 3.

5.2 Future Work

The following are tasks which must be pursued in order to complete this project:

- The dependence of the 1.53 μm laser on current and why it is not linear, should be fully understood.

- The tuning fork should be characterized in various concentrations of NH_3 in order to fully determine the relationship between sample concentration and damping. Although it was assumed previously that the shift in resonance frequency should be negligible at trace concentrations, this should be verified as well.

- A model should be developed which predicts absorption peak signals as a function of pressure and temperature. This would involve thoroughly understanding the Voigt profile.

Bibliography

[1] Jean-Phillipe Besson. *Photoacoustic Spectroscopy For Multi-Gas Sensing Using Near Infrared Lasers.* PhD thesis, Ecole Polytechnique Federale de Lausanne, 2006.

[2] Theodore L. Brown and Catherine Murphy. *Chemistry: the central science.* Pearson Education International, 2008.

[3] Steven D. Campbell, Sinclair S. Yee, and Martin A. Afromowitz. Applications of photoacoustic spectroscopy to problems in dermatology research. *IEEE Transactions on Biomedical Engineering Journal*, (4):220–227, April 1979.

[4] W. Demtroder. *Laser Spectroscopy: Basic Concepts and Instrumentation.* Springer, 1996.

[5] A.A. Kosterev et al. Quartz-enhanced photoacoustic spectroscopy. *Optics Letters Journal*, 27(21):1902–1904, nov 2002.

[6] Agnes Grossel et al. Photoacoustic detection of nitric oxide with a helmholtz resonant quantum cascade laser sensor. *Infrared Physics and Technology Journal*, 51(12):95–101, January 2007.

[7] F.J.M. Harren et al. On-line laser photoacoustic detection of ethene in exhaled air as biomarker of ultraviolet radiation damage of the human skin. *Applied Physics Letters Journal*, 74(12):1761–1763, March 1999.

[8] Frans J.M. Harren et al. Photoacoustic spectroscopy in trace gas monitoring. In R.A. Meyers, editor, *Encyclopedia of Analytical Chemistry*, number 23 in Fast Computers, part 3, pages 179–183. John Wiley and Sons Ltd, Chichester, third edition, September 2000.

[9] Lundsberg-Nielsen et al. *Journal of Molecular Spectroscopy Journal*, 47(1):230–245, January 1993.

[10] M. Horstjann et al. Formaldehyde sensor using interband cascade laser based quartz-enhanced photoacoustic spectrscopy. *Journal of Applied Physics B Journal*, 79(12):799–803, October 2004.

[11] Michael E. Webber et al. Agricultural ammonia sensor using diode lasers and photoacoustic spectroscopy. *Measurement Science and Technology Journal*, 16(12):1547–1553, June 2005.

[12] V. Zeninari et al. Methane detection on the sub-ppm level with a near-infrared diode laser photoacoustic sensor. *Infrared Physics and Technology Journal*, 44(1):253–261, February 2003.

[13] Samara Firebaugh. *Miniaturization and Intregration of Photoacoustic Detection.* PhD thesis, Massachusetts Institute of Technology, 2001.

[14] C. Fischer, R Bartlome, and S.W. Sigrist. The potential of mid-infrared photoacoustic spectroscopy for the detection of various doping agents used by athletes. *Journal of Applied Physics B Journal*, 85(1):289–294, July 2006.

[15] Hermann Haken and Hans C. Wolf. *Physics of Atoms and Quanta: Introduction to Experiments and Theory.* Springer, 2005.

[16] Anatoliy A. Kosterev and Frank K. Tittel. Ammonia detection by use of quartz-enhanced photoacoustic spectroscopy with a near-ir telecommunication diode laser. *Journal of Applied Optics Journal*, 43(33):6213–6217, November 2004.

[17] Sarah L.Gilbert and William C. Swann. Hydrogen cyanide absorption reference for 1530-1560 nm wavelength calibration. *NIST Special Publication Journal.*

[18] Courtesy of Dr. Harry Lee.

[19] John Richardson and Guybert Cahoon. *Methods and Materials For Teaching General and Physical Science.* McGraw-Hill, 1951.

[20] Allan Rosenswaig and Allen Gerscho. Theory of the photoacoustic effect with solids. *Journal of Applied Physics Journal*, 47(1):64–69, January 1976.

[21] Andreas Schmohl, Andras Miklos, , and Peter Hess. Detection of ammonia by photoacoustic spectroscopy with semiconductor lasers. *Journal of Applied Optics Journal*, 41(9):1815–1823, November 2002.

[22] Stephen D Senturia. *Microsystem Design.* Kluwers Academic Publishers, 1981.

[23] M. Wolff, M. Germer, H.G. Groninga, and H. Harde. Photoacoustic co_2 sensor based on a dfb diode laser at 2.7 μm. *The European Physical Journal Journal*, 151(9):409–413, March 2008.